Supplementary Information to accompany:

Slow magnetisation relaxation in tetraoxolene-bridged rare-earth complexes

Maja A. Dunstan,[a] Elodie Rousset,[a] Marie-Emmanuelle Boulon,[b] Robert W. Gable,[a] Lorenzo Sorace[b] and Colette Boskovic*[a]

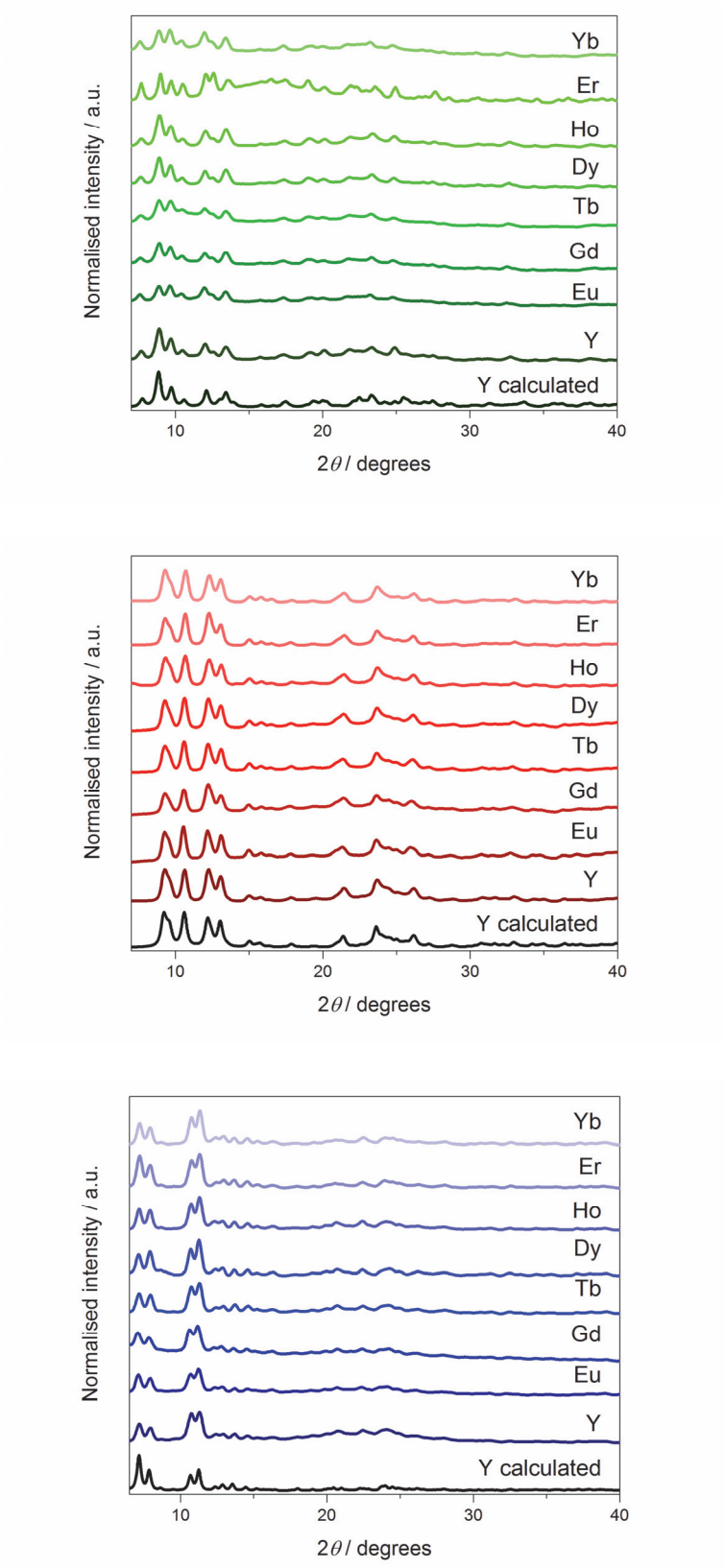

Fig. S1 Powder X-ray diffraction data for **1-RE**·$2CH_2Cl_2$ (top), **2-RE**, (middle) and **3-RE**·$x CH_2Cl_2$ (bottom, x = 0-2).

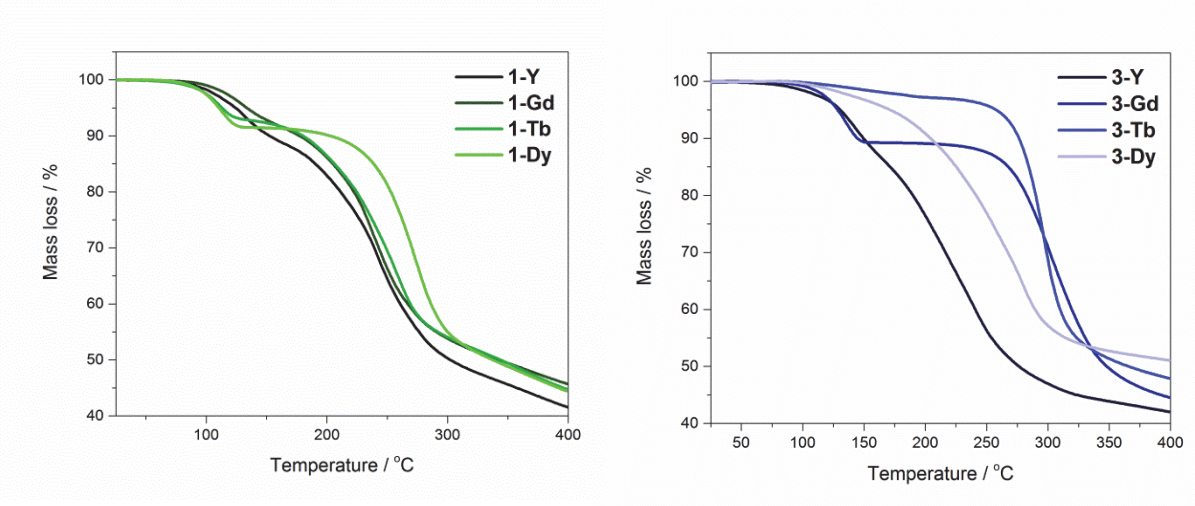

Fig. S2 Thermogravimetric analysis data for **1-RE**·2CH_2Cl_2 (left) and **3-RE**·*x*CH_2Cl_2 (right) at a ramp rate of 5°C min^{-1}.

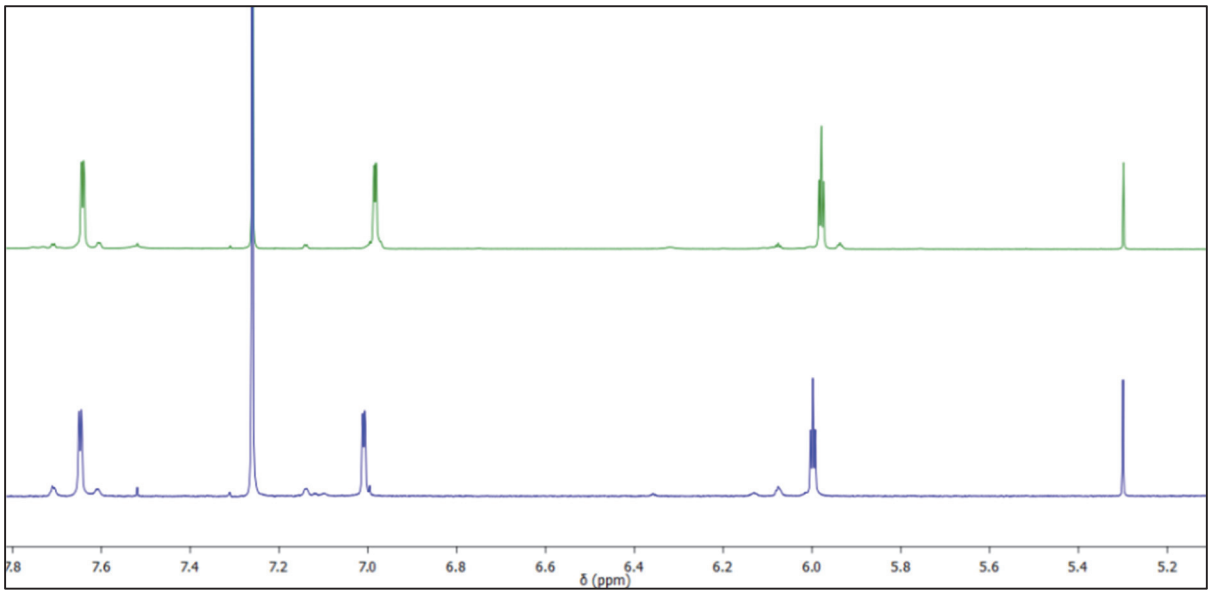

Fig. S3 ^{1}H NMR spectra of **1-Y**·2CH_2Cl_2 (top) and **3-Y**·1.2CH_2Cl_2 (bottom) in $CDCl_3$, showing the CH_2Cl_2 solvent peak at 5.3 ppm.

Table S1 SHAPE parameters for the rare earth centres in **1-Y**·2Me_2CO, **1-Y**·2CH_2Cl_2, **Dy**·2CH_2Cl_2, **2-Y**, **3-Y**·1.2CH_2Cl_2, **4-Y**·3.5MeOH and **5-Y**·5MeOH.

Shape parameter[a]	**1-Y**·2Me_2CO	**1-Y**·2CH_2Cl_2	**1-Dy**·2CH_2Cl_2	**2-Y**	**3-Y**·1.2CH_2Cl_2	**4-Y**·3.5MeOH	**5-Y**·5MeOH
Square antiprism	1.818	2.174	2.254	**0.801**	**0.594, 0.720**	1.950	2.216, 1.710
Triangular dodecahedron	**0.900**	**0.763**	**0.774**	1.242	2.447, 1.655	**1.414**	**1.216, 1.622**

[a] The closer the index to zero, the less the distortion from the ideal symmetry.[1,2]

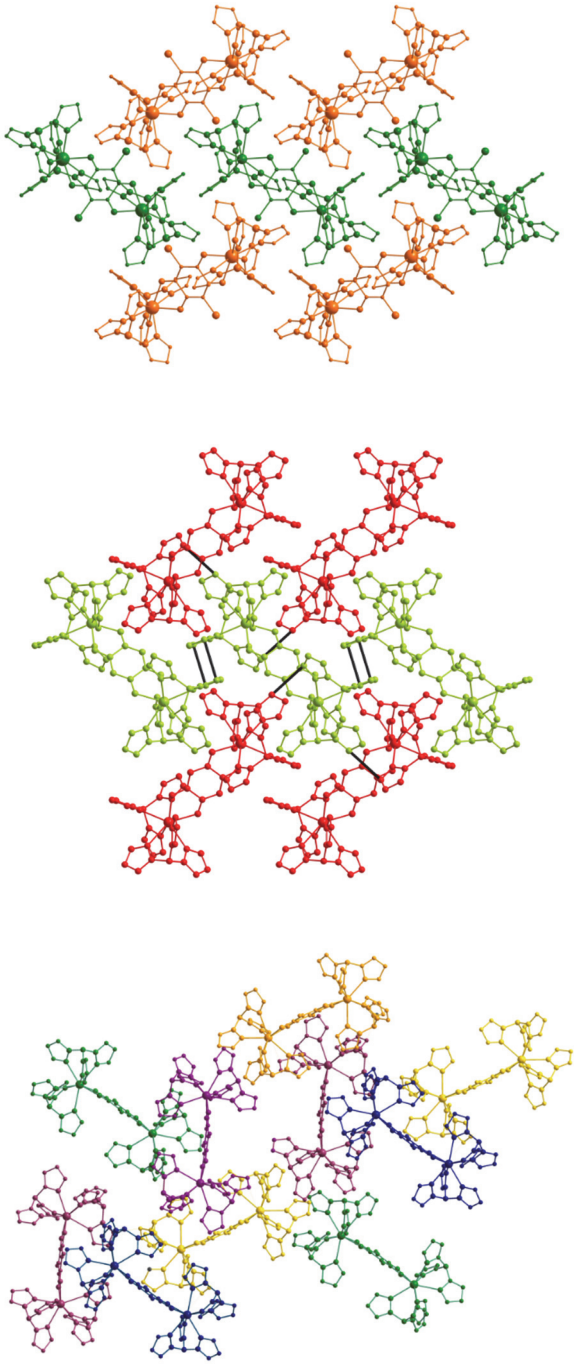

Fig. S4 Crystal packing diagrams for **1-Y**·2Me_2CO (top), **2-Y** (middle) and **3-Y**·1.2CH_2Cl_2 (bottom); solvent has been omitted for clarity.

Table S2 Selected interatomic distances (Å) for **4-Y**·3.5MeOH and **5-Y**·5MeOH.

Distance[a]	**4-Y**·3.5MeOH	**5-Y**·5MeOH	
		Y_1	Y_2
Y-O$_1$ (O$_3$)	2.3379(26)	2.2866(24)	2.3033(26)
Y-O$_2$ (O$_4$)	2.3521(26)	2.3708(26)	2.3398(23)
Y-O$_3$ (O$_5$, O$_7$)	2.3210(24)	2.3224(24)	2.3853(23)
Y-O$_4$ (O$_6$, O$_8$)	2.3509(31)	2.3963(21)	2.3414(22)
Y-O$_{MeOH}$	2.3429(31)	2.3173(27)	2.3654(28)
Y-N$_2$ (N$_8$)	2.4483(32)	2.4505(25)	2.4317(26)
Y-N$_4$ (N$_{10}$)	2.4745(44)	2.4659(32)	2.4683(33)
Y-N$_6$ (N$_{12}$)	2.4952(30)	2.5095(31)	2.4798(31)
O$_1$-C$_{10}$ (C$_{19}$)	1.2600(47)	1.2701(40)	
O$_2$-C$_{12}$ (C$_{20}$)	1.2677(44)	1.2587(39)	
C$_{11}$-C$_{12}$ (C$_{19}$-C$_{21}$)	1.4003(55)	1.3961(44)	
C$_{10}$-C$_{12}$ (C$_{21}$-C$_{23}$)	1.5263(62)	1.4010(53)	
Intramolecular Y···Y	8.5765(9)	6.0860(5)	
Intermolecular Y···Y[2]	8.3188(8)	9.7290(6)	

[a] In brackets are corresponding atom labels for **5-Y**·5MeOH

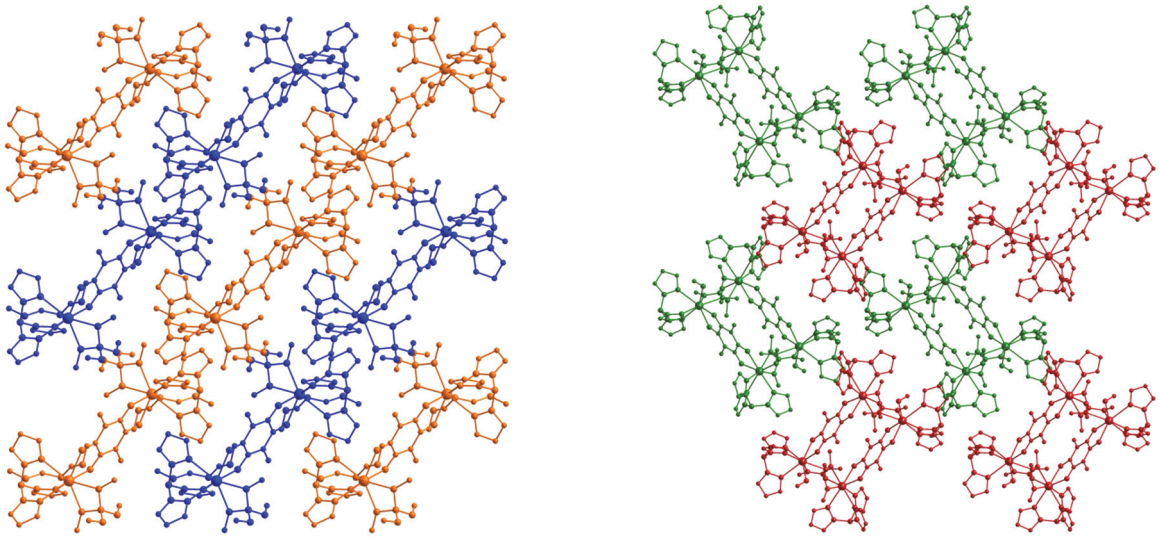

Fig. S5 Crystal packing diagrams for **4-Y**·3.5MeOH (left) and **5-Y**·5MeOH (right) ; solvent and counterions have been omitted for clarity.

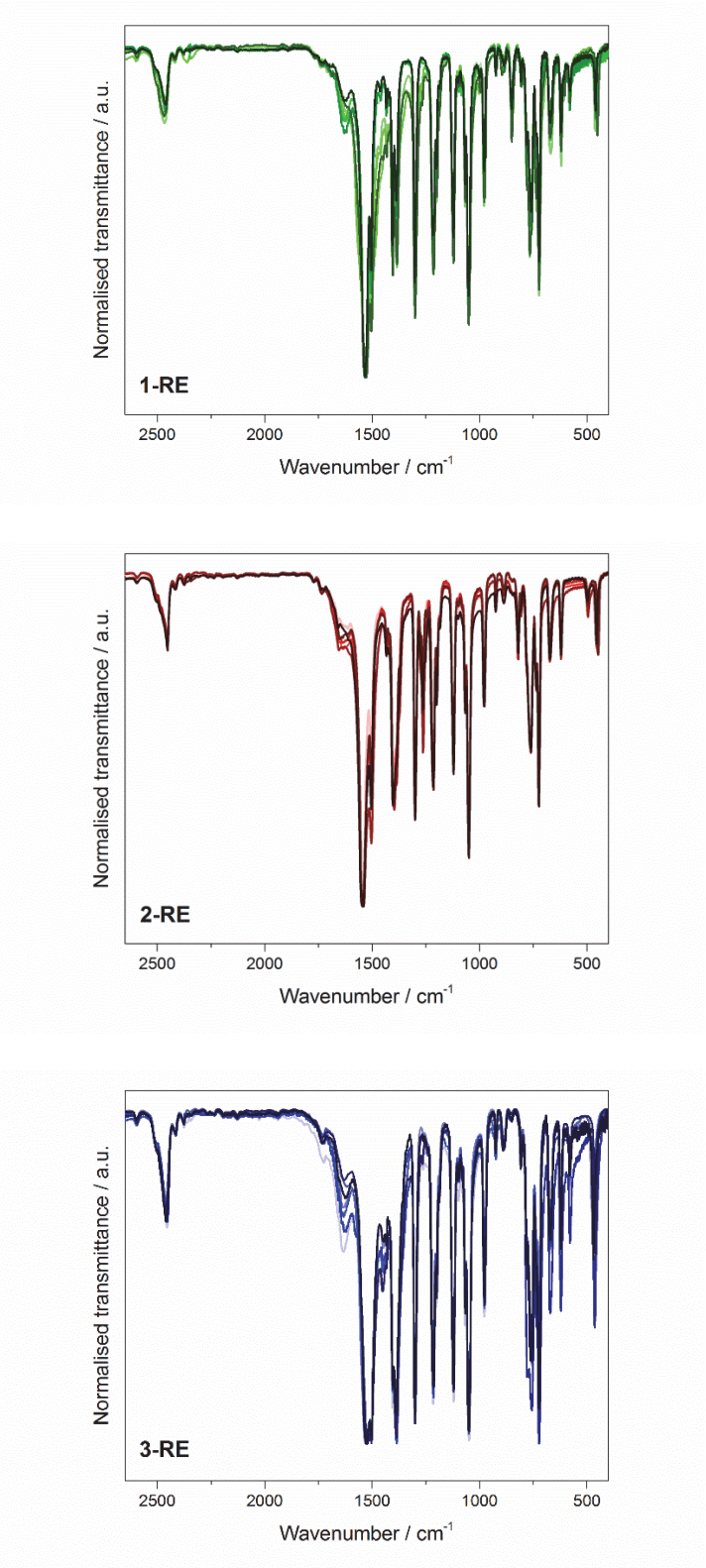

Fig. S6 Infrared spectra of **1-RE**·2CH_2Cl_2 (top), **2-RE** (middle) and **3-RE**·*x*CH_2Cl_2 (bottom) as KBr disks; the spectra are coloured from Y (darkest) to Yb (lightest).

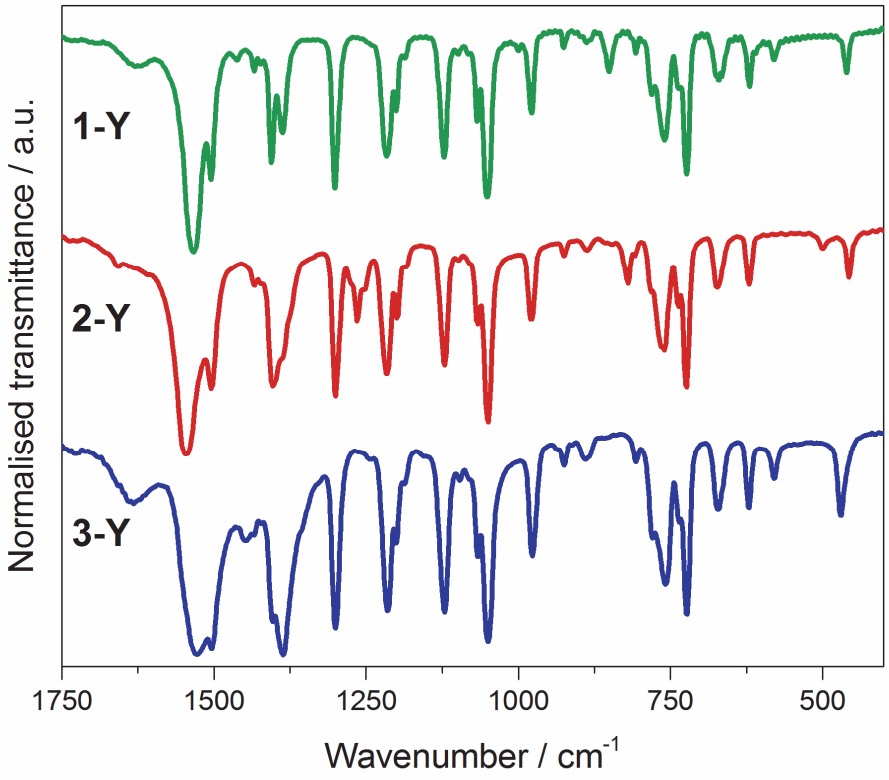

Fig. S7 Comparison of infrared spectra in the fingerprint region 400–1750 cm^{-1} for **1-Y**, **2-Y** and **3-Y**.

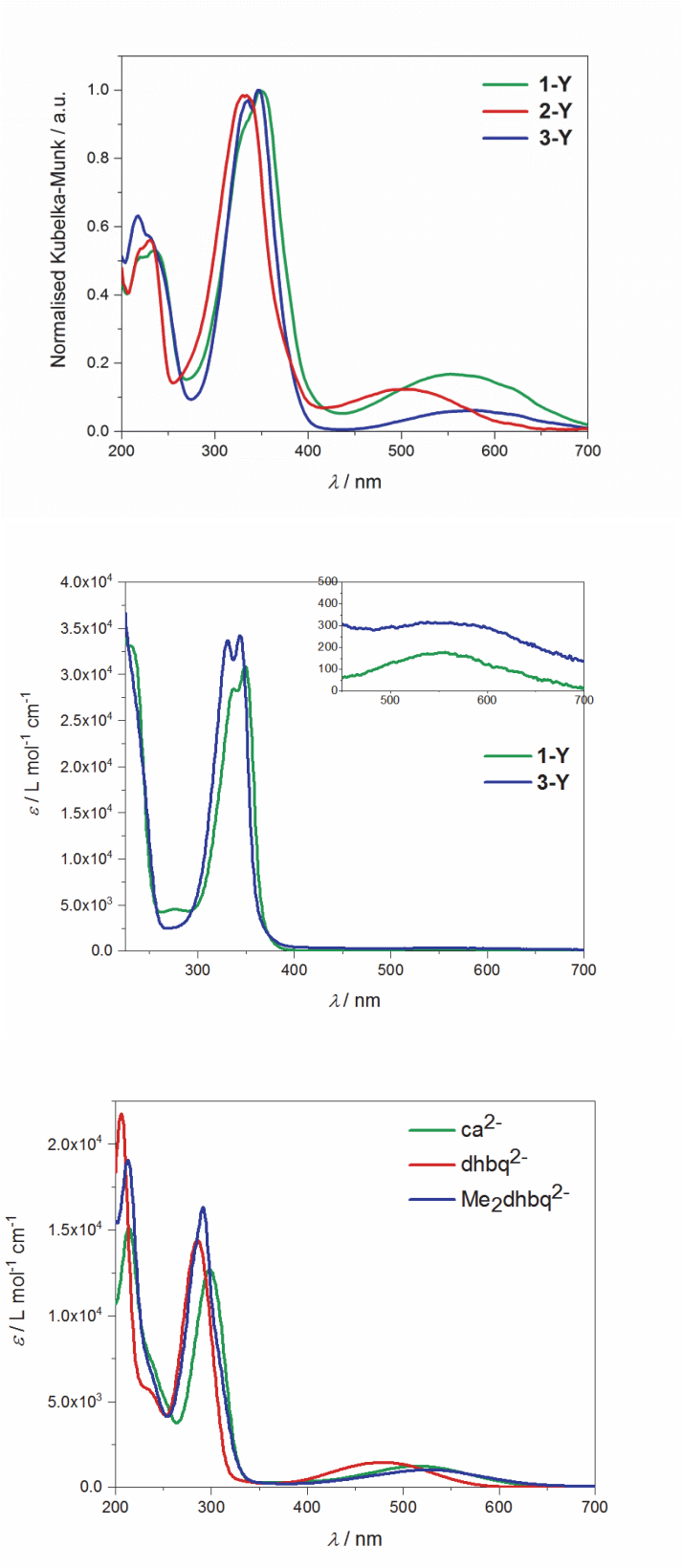

Fig. S8 Electronic spectra for **1-Y**, **2-Y** and **3-Y** measured as diffuse reflectance dispersed in KBr (top) and for **1-Y** and **3-Y** as absorbance in acetonitrile (middle) with absorbance spectra of the doubly deprotonated tetraoxolene ligands for comparison (bottom).

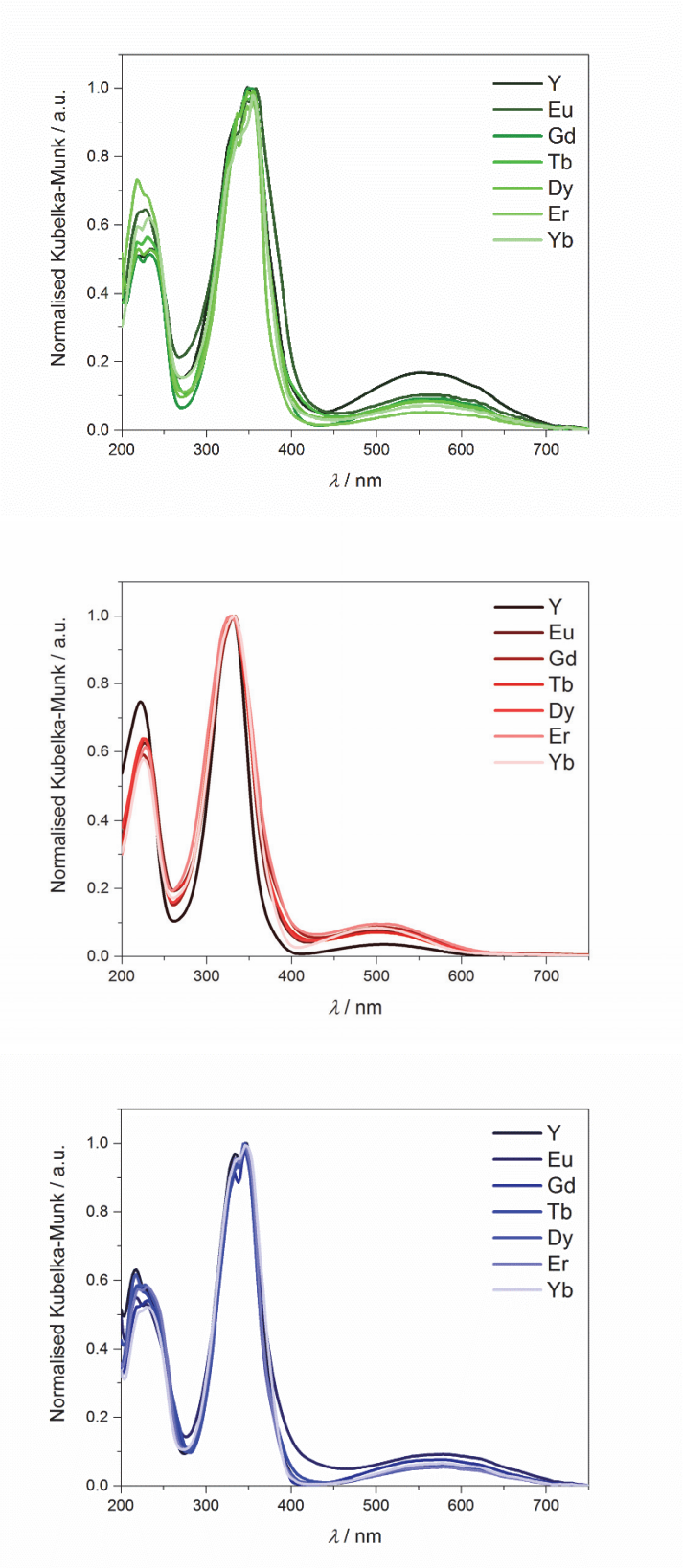

Fig. S9 Diffuse reflectance spectra for the different members of the **1-RE**·2CH_2Cl_2 (top), **2-RE** (middle) and **3-RE**·*x*CH_2Cl_2 (bottom) families.

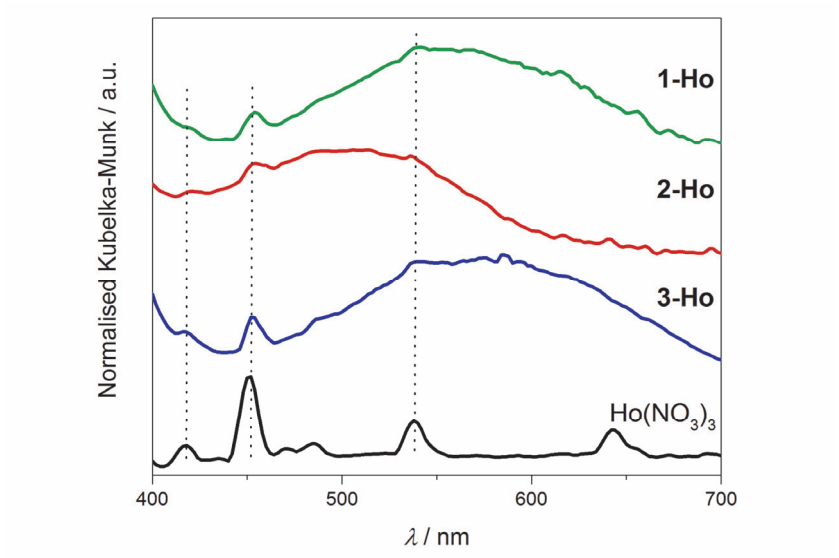

Fig. S10 Diffuse reflectance spectra for **1-Ho, 2-Ho, 3-Ho** and $Ho(NO_3)_3$.

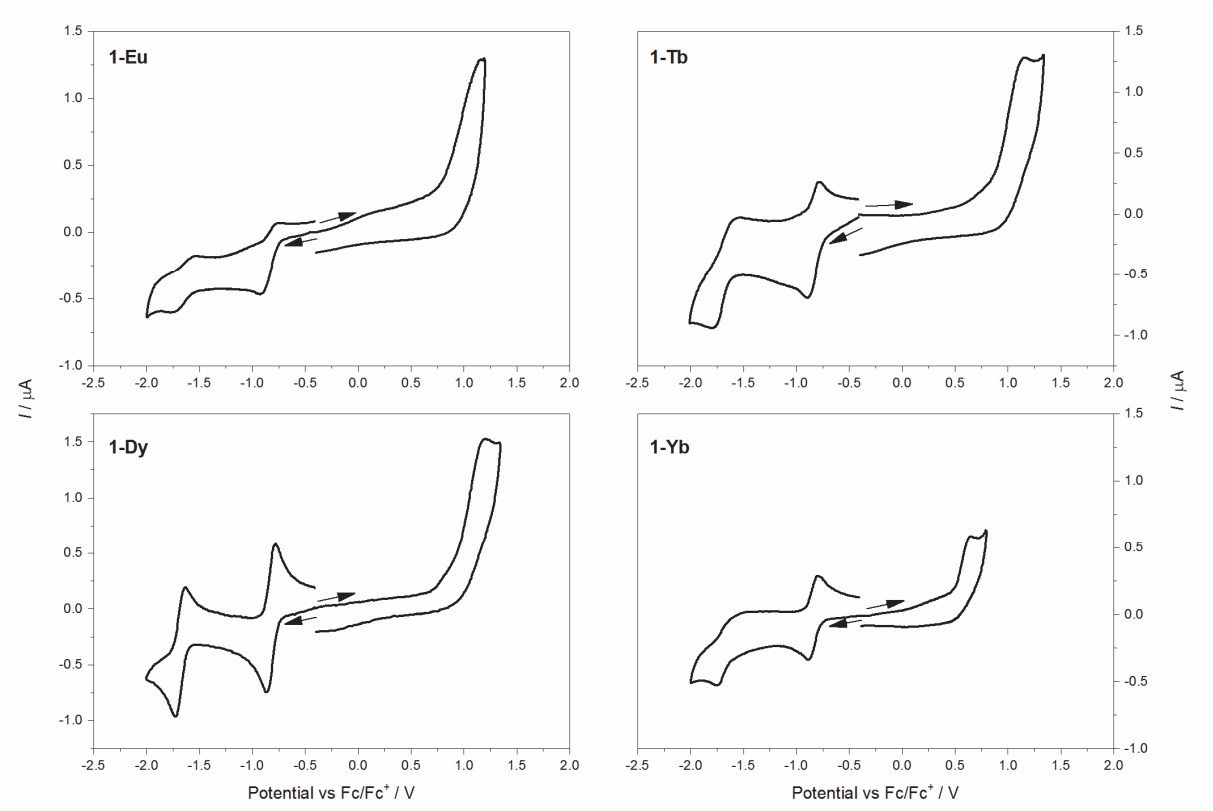

Fig. S11 Cyclic voltammograms of **1-RE** (RE = Eu, Tb, Dy, Yb; 0.5 mM in MeCN with 0.1 M Bu_4NPF_6) obtained with a 1 mm diameter glassy carbon working electrode at a scan rate of 100 mV/s. The anodic and cathodic regions were scanned separately as indicated by the arrows.

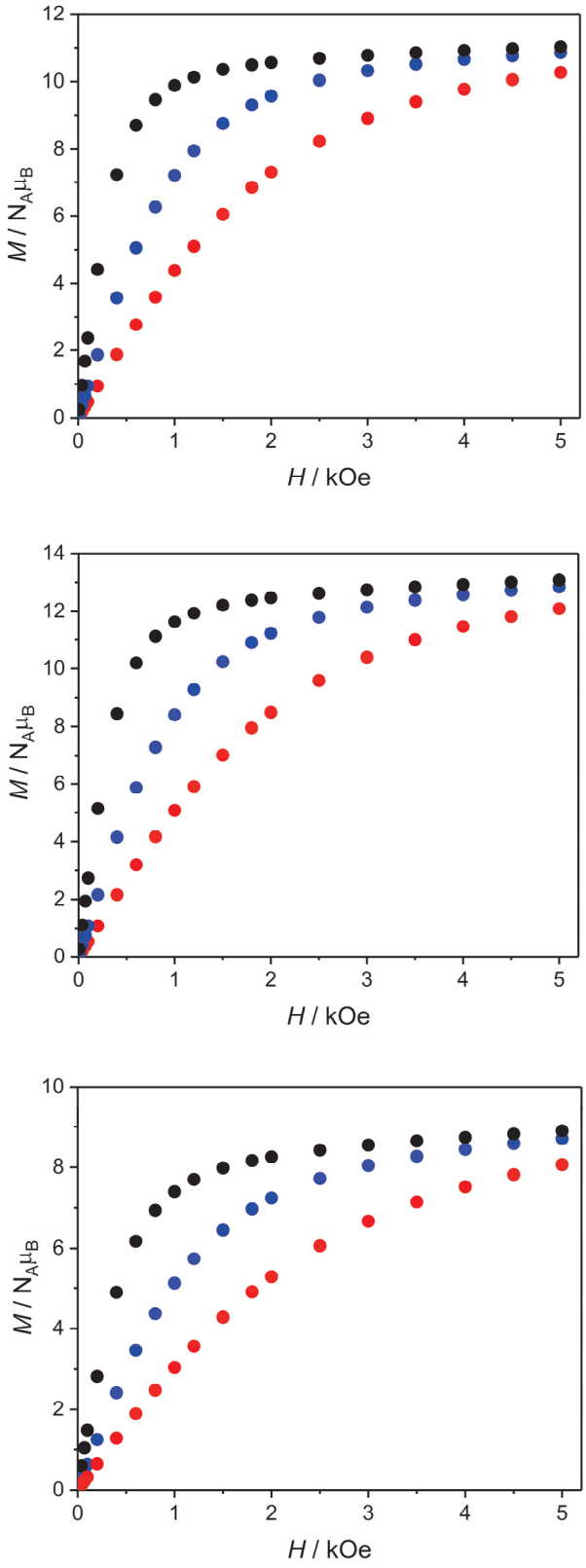

Fig. S12 Magnetisation versus field data at 2 (black), 5 (blue) and 10 K (red) for **1-Dy**·2CH_2Cl_2 (top), **3-Dy**·1.1CH_2Cl_2 (middle) and **3-Tb**·0.7CH_2Cl (bottom).

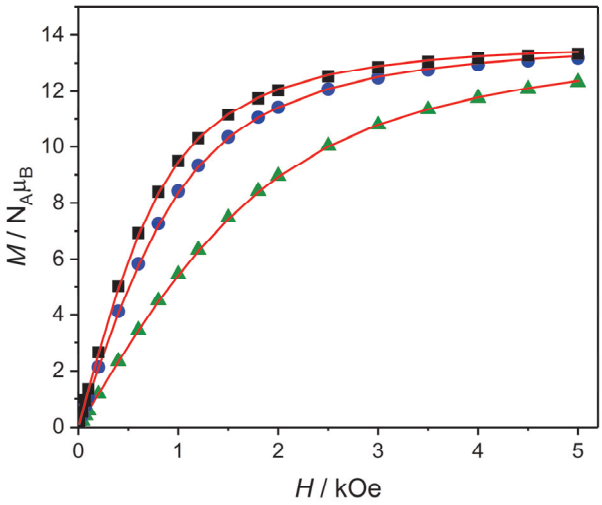

Fig. S13 Magnetisation versus field data at 2.0 (squares), 2.5 (circles) and 4.5 K (triangles) for **3-Gd**·$2CH_2Cl_2$ with the fit (lines) as described in the text.

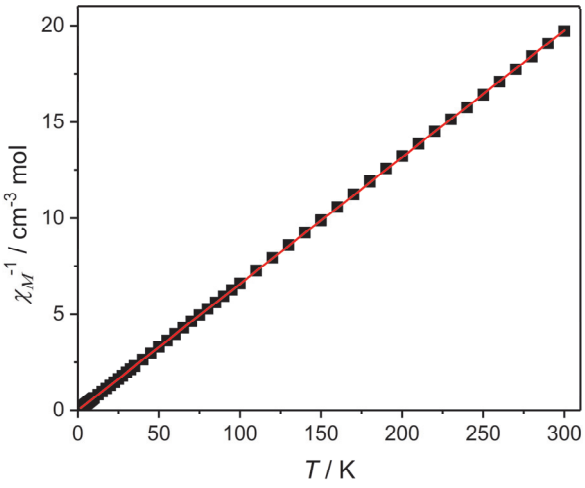

Fig. S14 Curie-Weiss plot and best fit (line) as described in the text for **3-Gd**·$2CH_2Cl_2$.

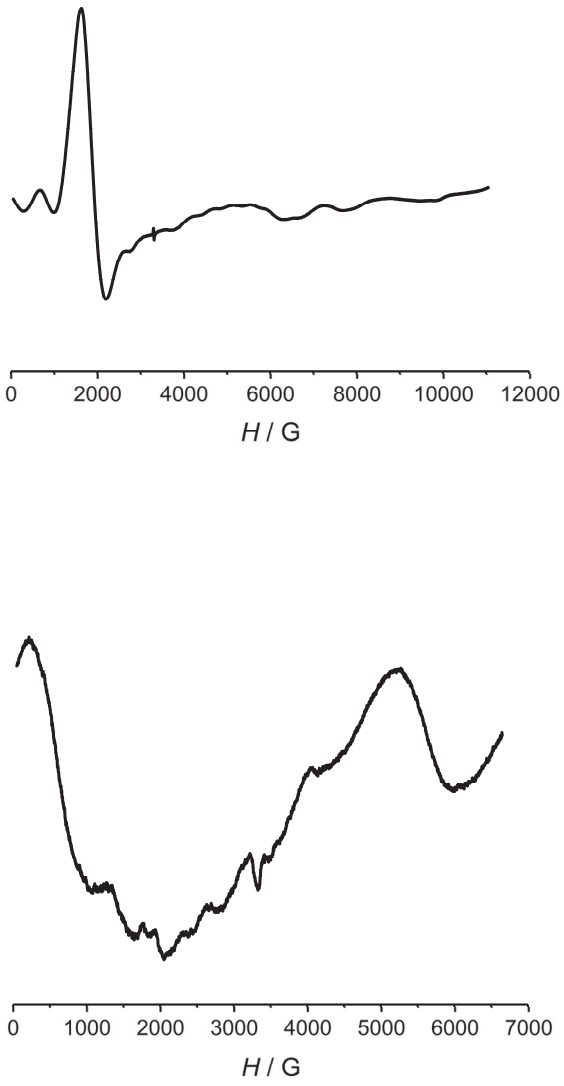

Fig. S15 X-band EPR spectra at 10 K for powder samples of **3-Gd**·2CH_2Cl_2 (top) and **3-Tb**·0.7CH_2Cl_2 (bottom).

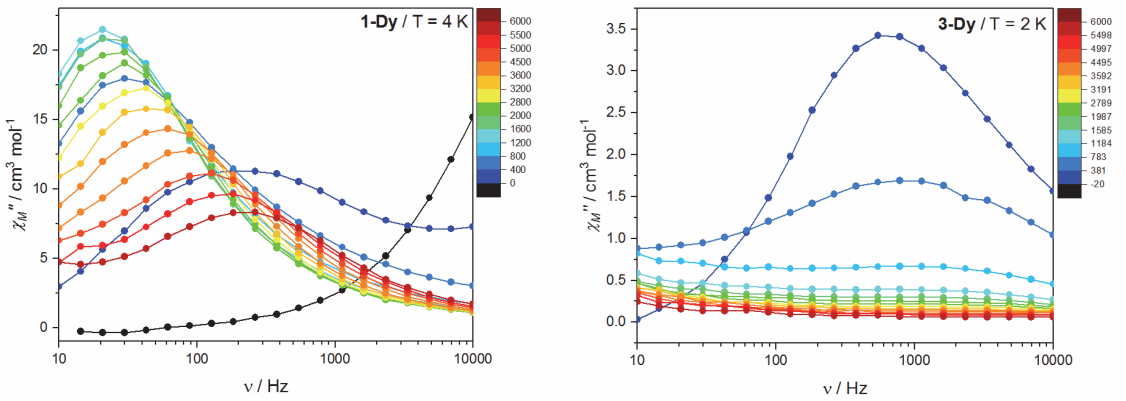

Fig. S16 Field (Oe) dependence of the out-of-phase ac magnetic susceptibility for **1-Dy**·2CH_2Cl_2 (left) and **3-Dy**·1.1CH_2Cl_2 (right) as a function of frequency at 4 or 2 K for **1-Dy** and **3-Dy**, respectively.

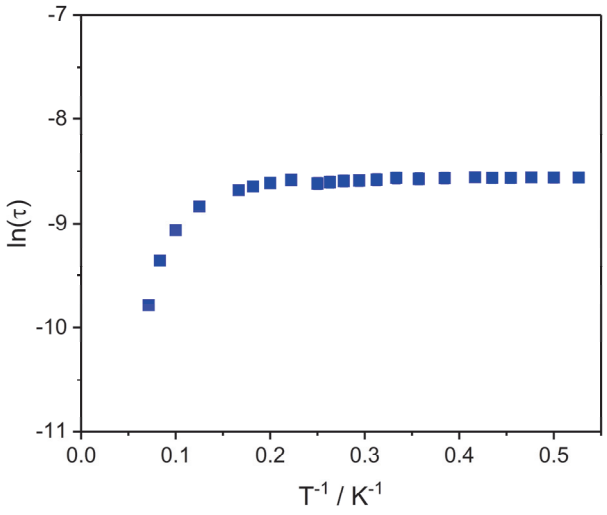

Fig. S17 Arrhenius plot of relaxation rates of **3-Dy**·1.1CH_2Cl_2 in zero applied dc magnetic field.

References

1 D. Casanova, M. Llunell, P. Alemany, S. Alvarez, P. D. Casanova, M Llunell and S. A. Alemany, *Chem. Eur. J.*, 2005, **11**, 1479.

2 M. Llunell, D. Casanova, J. Cirera, J. M. Bofill, P. Alemany, S. Alvarez, M. Pinsky and D. Avnir, *SHAPE 2.0*, Universitat de Barcelona and The Hebrew University of Jerusalem, Barcelona, 2003.